

## Water Splitting | Hot Paper |

## Epitaxial Cubic Silicon Carbide Photocathodes for Visible-Light-Driven Water Splitting

Xiuxiu Han,<sup>[a, b, c]</sup> Steffen Heuser,<sup>[c]</sup> Xili Tong,<sup>\*,[a]</sup> Nianjun Yang,<sup>\*,[c]</sup> Xiang-Yun Guo,<sup>[a, b, d]</sup> and Xin Jiang<sup>[c]</sup>

**Abstract:** Cubic silicon carbide (3C-SiC) material feature a suitable bandgap and high resistance to photocorrosion. Thus, it has been emerged as a promising semiconductor for hydrogen evolution. Here, the relationship between the photoelectrochemical properties and the microstructures of different SiC materials is demonstrated. For visible-light-derived water splitting to hydrogen production, nanocrystalline, microcrystalline and epitaxial (001) 3C-SiC films are applied as

the photocathodes. The epitaxial 3C-SiC film presents the highest photoelectrochemical activity for hydrogen evolution, because of its perfect (001) orientation, high phase purity, low resistance, and negative conduction band energy level. This finding offers a strategy to design SiC-based photocathodes with superior photoelectrochemical performances.

## Introduction

As a green renewable source, hydrogen is compelling for the advances in lifestyle of modern society, due to its high energy density and environmental benignity. A promising pathway for hydrogen production is the photoelectrochemical (PEC) water splitting driven by solar energy,<sup>[1]</sup> which represents an ideal and sustainable strategy to the clean and efficient energy challenge. To achieve the practical applications of PEC for water splitting, efficient and stable catalysts are vital to promote the sluggish kinetics of water decomposition. In particular, PEC catalysts must own both photocatalytic and electrocatalytic activity and durability.<sup>[2]</sup> A number of semiconductors, such as

TiO<sub>2</sub>,<sup>[3]</sup> Cu<sub>2</sub>O,<sup>[4]</sup> and CdS,<sup>[5]</sup> have been employed as potential photocathodes, inspired by their high photoresponse and admissible conductivity.<sup>[6]</sup> Unfortunately, their shortcomings (e.g., too broad bandgaps,<sup>[7]</sup> easily causticity,<sup>[8]</sup> poor stability,<sup>[9]</sup> or the low catalytic efficiencies<sup>[10]</sup>) limit their performances and large-scale applications. Therefore, the design and construction of high-performance visible-light-driven PEC catalysts are highly desired.

To boost PEC water splitting for hydrogen generation, the bottom of the conduction band of a semiconductor catalyst has to be more negative than the reduction potential of H<sup>+</sup>/H<sub>2</sub>. A higher conduction band position presents greater reduction ability. Among various semiconductors, a 3C-SiC film exhibits the highest conduction band position with a bandgap of 2.4 eV, indicating the superior photoreduction ability under visible-light irradiation.<sup>[11]</sup> Moreover, it possesses fast charge-transfer rates, excellent corrosion resistance, and high electrocatalytic activity for H<sub>2</sub> production.<sup>[2a,12]</sup> Therefore, a photocathode of a 3C-SiC film is expected to present outstanding PEC water splitting performance under the visible-light irradiation. Furthermore, the direct employment of a 3C-SiC film avoids the usage of organic binders in the case of SiC nanoparticles. The reports on PEC water splitting using 3C-SiC films are actually seldom, mainly due to the complex processes during the synthesis of 3C-SiC films.<sup>[13]</sup>

In this work, an epitaxial 3C-SiC film with perfect (001) orientation and high phase purity was prepared and further applied as the photocathode for PEC water splitting in acidic electrolyte. In this case, the surface of an epitaxial 3C-SiC film owns numerous catalytic activity sites (i.e., terminal Si sites) that are available for hydrogen evolution reaction (HER). In addition, low photoinduced charge recombination can take place, due to a short transfer distance and scarce defects. To verify the advances of an epitaxial 3C-SiC film for PEC water splitting, syn-

[a] X. Han, Dr. X. Tong, Prof. Dr. X.-Y. Guo  
State Key Laboratory of Coal Conversion  
Institute of Coal Chemistry, Chinese Academy of Sciences  
Taiyuan 030001 (P. R. China)  
E-mail: tongxili@sxicc.ac.cn

[b] X. Han, Prof. Dr. X.-Y. Guo  
Center of Materials Science and Optoelectronics Engineering  
University of Chinese Academy of Sciences  
Beijing 100049 (P. R. China)

[c] X. Han, S. Heuser, Dr. N. Yang, Prof. Dr. X. Jiang  
Institute of Materials Engineering, University of Siegen  
Siegen 57076 (Germany)  
E-mail: nianjun.yang@uni-siegen.de

[d] Prof. Dr. X.-Y. Guo  
School of Petrochemical Engineering, Changzhou University  
Changzhou 213164 (P. R. China)

Supporting information and the ORCID identification number(s) for the author(s) of this article can be found under:  
<https://doi.org/10.1002/chem.201905218>.

© 2020 The Authors. Published by Wiley-VCH Verlag GmbH & Co. KGaA. This is an open access article under the terms of Creative Commons Attribution NonCommercial License, which permits use, distribution and reproduction in any medium, provided the original work is properly cited and is not used for commercial purposes.

thesized microcrystalline and nanocrystalline 3C-SiC films (see the Supporting Information for details) were also applied for PEC water splitting.

## Results and Discussion

Figure 1 shows the scanning electron microscopy (SEM) images of nanocrystalline (Figure 1a), microcrystalline (Figure 1b), and epitaxial (Figure 1c) 3C-SiC films. The average crystal size of a nanocrystalline 3C-SiC film is smaller than 50 nm, and its surface is relatively smooth (Figure 1a). In contrast, the average crystal size of a microcrystalline 3C-SiC film is larger than 200 nm (Figure 1b), and its surface is higher roughness in comparison to that of a nanocrystalline 3C-SiC. For an epitaxial 3C-SiC film, densely packed 3C-SiC crystals grow along the  $\langle 110 \rangle$  directions, which is attributed to the heteroepitaxial growth of 3C-SiC crystals on a (001) Si substrate.<sup>[12–13]</sup>

The XRD patterns of a 3C-SiC film with  $2\theta$  position of 35.6, 41.4, 62.0, and 90.0° are indexed to the (111), (200), (220), and (400) of 3C-SiC, respectively (JCPDS No. 29–1129, Figure S1a, Supporting Information). In case of an epitaxial 3C-SiC film, the diffraction of (200) and (400) are stronger, an indication of its perfect (001) orientation. Briefly, an epitaxial 3C-SiC film consists of single 3C-SiC crystals which feature no amorphous phases. Differently, (111) plane is also observed in a nanocrystalline 3C-SiC film and a microcrystalline 3C-SiC film, indicating their polycrystalline nature. In addition, Raman analysis was also carried out to examine the phase purity of these films (Figure S1b, Supporting Information). There are two significant differences among nanocrystalline, microcrystalline and epitaxial 3C-SiC films. Firstly, for nanocrystalline and microcrystalline 3C-SiC films, the peaks at approximately 1320 (D band) and 1600  $\text{cm}^{-1}$  (G band) indicate the presence of amorphous carbon phase in both films. Secondly, the weak and broad peak at about 900  $\text{cm}^{-1}$  is ascribed to the Si–C rocking in Si-CH<sub>3</sub>, implying the existence of the amorphous SiC phase in both films. However, these three peaks are not observable in the case of an epitaxial 3C-SiC film. This contrast suggests no amorphous phase, but the only existence of 3C-SiC crystals in an epitaxial 3C-SiC film, indicating clearly its high phase purity. Such a result is in good accordance with our previous transmission electron microscopy (TEM) observation.<sup>[12]</sup> Moreover, a slight downshift is seen in the position of a SiC TO peak for a microcrystalline SiC film when compared with that for a nano-

crystalline SiC film, confirming its better crystallinity. The crystallinity increases in the order of nanocrystalline < microcrystalline < epitaxial. These structural characterization results confirm the perfect (001) orientation and high phase purity of an epitaxial 3C-SiC film.

According to the report by Demichelis et al., the amorphous phases restrain the electron transfer between the SiC crystals.<sup>[14]</sup> Therefore, the electrical conductivity of an epitaxial 3C-SiC film derived from high purity is expected to be higher than that of a nanocrystalline 3C-SiC film or a microcrystalline one. To confirm this statement, the sheet resistance was calculated through a four-point-probe technique. The obtained sheet resistance of an epitaxial 3C-SiC film is as low as about 86  $\Omega\text{sq}^{-1}$ . In contrast, the nanocrystalline and microcrystalline 3C-SiC films show the sheet resistances of about 678 and 578  $\Omega\text{sq}^{-1}$ , respectively. Consequently, an epitaxial 3C-SiC film is expected to feature outstanding performance of PEC water splitting.

Prior to employing these 3C-SiC films for PEC water splitting, the optical behavior of an epitaxial 3C-SiC film was investigated by means of UV/Vis diffuse-reflectance spectroscopy. The epitaxial 3C-SiC film exhibits a broad and strong adsorption peak in UV- and visible-light regions. An absorption edge appears at approximately 520 nm (Figure 2a). From the redrawn Tauc plot (Figure 2b), its bandgap was estimated by extrapolating the slope and the  $E_g$  value. The estimated value is approximately 2.5 eV. This corresponds to the broad absorption region between 330 and 520 nm. The different bandgaps between an epitaxial 3C-SiC film and 3C bulk SiC (e.g., 2.4 eV) is probably due to the highly pure nature of an epitaxial 3C-SiC film.<sup>[15]</sup> The flat-band potential was then determined by impedance measurements. As seen from the Mott–Schottky plot ( $1/C^2$  vs.  $V$ ) for an epitaxial 3C-SiC film at a frequency of 1 kHz (Figure 1c), the slope of the linear range is negative, indicating a p-type conductive behavior.<sup>[16]</sup>

The flat-band potential, determined by extrapolating the Mott–Schottky plot to  $1/C^2=0$ , is 1.1 V (vs. Ag/AgCl), namely 1.3 V (vs. SHE). Provided that the valence band is 0.1 V more positive than the flat band potential,<sup>[17]</sup> the valence band (VB) of an epitaxial 3C-SiC film is 1.4 V (vs. SHE). The estimated conduction band (CB) is then  $-1.1$  V (vs. SHE), according to  $E_g = |E_{\text{CB}} - E_{\text{VB}}|$ . Such an energy level diagram of an epitaxial 3C-SiC film is schematically shown in Figure 2d, in which it is further compared with the redox potentials of water splitting reac-

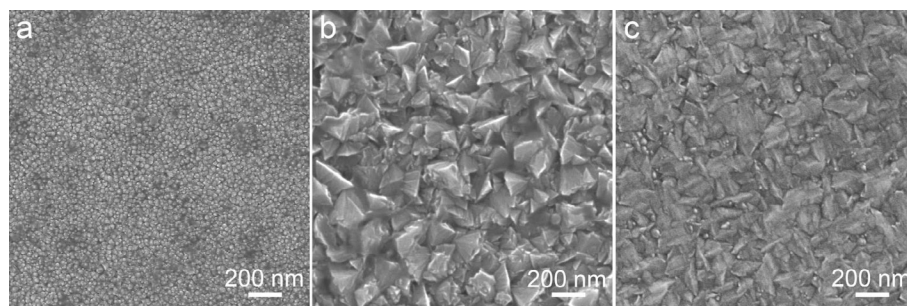
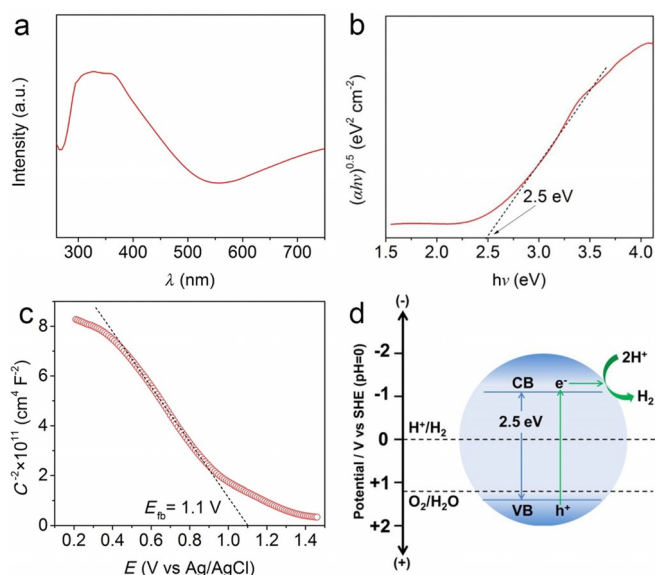


Figure 1. SEM images of (a) nanocrystalline, (b) microcrystalline, and (c) epitaxial 3C-SiC films.



**Figure 2.** Optical properties of an epitaxial 3C-SiC film: (a) UV/Vis diffuse-reflectance spectrum, (b) the redrawn Tauc plot from (a), (c) Mott-Schottky plot collected at a frequency of 1.0 kHz in 0.5 M H<sub>2</sub>SO<sub>4</sub> in the dark, and (d) energy diagram compared with redox potentials for water splitting. In (d), electrochemical energy scale (left) is relative to the standard hydrogen electrode (SHE). Black dotted lines represent the water-splitting energies for hydrogen evolution [E(H<sup>+</sup>/H<sub>2</sub>O)] and oxygen evolution [E(O<sub>2</sub>/H<sub>2</sub>O)] in pH 0 solutions.

tions. Clearly, the CB edge is situated above the reduction energy level of water splitting, E(H<sup>+</sup>/H<sub>2</sub>O). Taking the facts of its relatively high conductivity and broad UV/Vis absorption into account, an epitaxial 3C-SiC film is ideal for PEC water splitting or hydrogen production.

The PL spectra were then recorded to explore the photo-generated charge recombination on three SiC films (Figure S2, Supporting Information). The PL emission signal of an epitaxial 3C-SiC film is significantly weaker than that of nanocrystalline and microcrystalline 3C-SiC films. This is due to the notable depression of recombination of the photogenerated charge carriers on an epitaxial 3C-SiC film, which actually benefits to the separation of electrons and holes.<sup>[18]</sup> This is highly desirable to improve photocatalytic activity of 3C-SiC films.

The catalytic ability and photo-response of an epitaxial 3C-SiC film (labeled as epi) were then examined by means of tran-

sient photocurrent measurements. These tests were carried out by means of linear sweep voltammetry (LSV) under chopped light illumination. An epitaxial 3C-SiC film presents a higher current density than other 3C-SiC films for hydrogen evolution from water splitting under simulative sun light irradiation (Figure 3a). The current density is as high as 20 mA cm<sup>-2</sup> at a potential of -1.0 V (vs. Ag/AgCl) under the similar conditions.<sup>[19]</sup> Moreover, this epitaxial 3C-SiC photocathode displays prompt and reproducible photocurrent response with respect to the ON-OFF cycles of the irradiation signal, indicating obviously enhanced photocatalytic activity. To explore the effect of scan rate on PEC performance of an epitaxial 3C-SiC film, *J*-*V* curves were recorded under chopped light illumination at the scan rates of 5, 10, 15, 20 and 25 mV s<sup>-1</sup> (Figure S3, Supporting Information). An increase of scan rate results in enhanced current density and photocurrent response. To evaluate PEC stability of this epitaxial 3C-SiC film photocathode, its amperometric response (*I*-*t* curve) was recorded (Figure 3b), depicting the fast response toward irradiation stimulation. The square profile and steady photocurrent density of transient photocurrent response (more than 25 cycles) further indicate a fast surface reduction kinetics, suppressed charge carrier recombination, and remarkable PEC stability.<sup>[20]</sup> EIS measurements were thus conducted to investigate the charge transport behavior of an epitaxial 3C-SiC photocathode. From the recorded Nyquist plots (Figure 3c) and the electric circle (inset in Figure 3c), its calculated charge transfer resistance (*R*<sub>ct</sub>) under light illumination is 17 Ω, smaller than that without illumination. This suggests again that photoinduced electrons are engaged in the electron transfer across the photoelectrode/solution interface.

For comparison, the HER performances of nanocrystalline (labeled as nano) and microcrystalline (labeled as micro) 3C-SiC photocathodes were also examined under identical conditions. As expected, nanocrystalline and microcrystalline photocathodes exhibit higher current densities under illumination than in the dark (Figure 4a). However, both current densities [6.2 mA cm<sup>-2</sup> for nano and 8.1 mA cm<sup>-2</sup> for micro at -1.0 V (vs. Ag/AgCl)] are lower than that of an epitaxial 3C-SiC photocathode under illumination [20 mA cm<sup>-2</sup> at -1.0 V (vs. Ag/AgCl)]. It has been stated that the microstructures of catalysts affect their catalytic reactivity.<sup>[21]</sup> The variation of these current densities toward HER on three photocathodes thus results from dif-

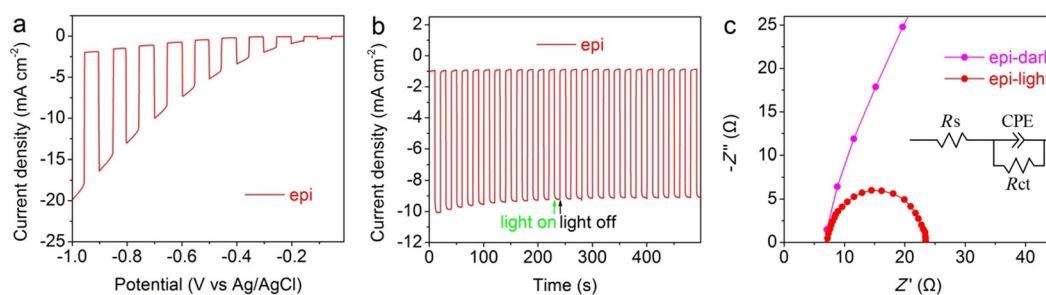


**Figure 3.** PEC performance of an epitaxial 3C-SiC photocathode toward HER: (a) the *J*-*V* curve under chopped light illumination, (b) *I*-*t* curve at -0.7 V (vs. Ag/AgCl) under chopped-light illumination, and (c) Nyquist plots recorded at -0.7 V (vs. Ag/AgCl) under light illumination (red line with dots) and in the dark (pink line with dots).

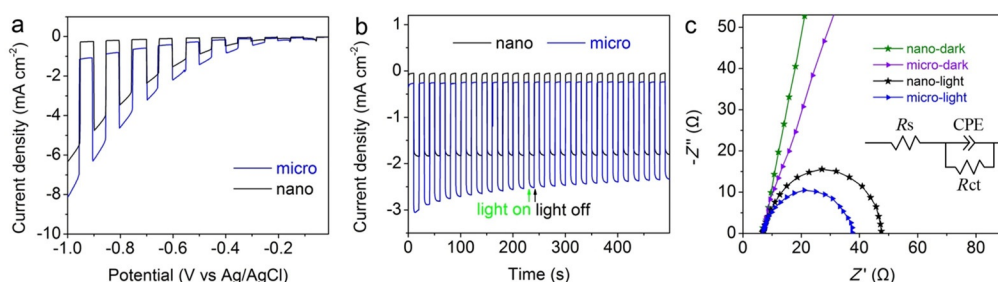


**Figure 4.** PEC performances of the nanocrystalline and microcrystalline 3C-SiC photocathodes toward HER: (a)  $J$ - $V$  curves under chopped light illumination, (b)  $I$ - $t$  curves at  $-0.7$  V (vs. Ag/AgCl) under chopped light illumination, and (c) Nyquist plots recorded at  $-0.7$  V (vs. Ag/AgCl) under light illumination for a microcrystalline film (the blue line with triangles) and for a nanocrystalline film (the black line with stars) as well as in the dark for a microcrystalline film (the green line with triangles) and for a nanocrystalline film (the purple line with stars).

ferent microstructures of three SiC films.<sup>[12]</sup> In addition,  $J$ - $V$  curves under chopped light illumination at different scan rates for microcrystalline (Figure S4, Supporting Information) and nanocrystalline (Figure S5, Supporting Information) 3C-SiC films also indicate current densities (namely better PEC response). Therefore, the perfect (001) orientation and the high phase purity of an epitaxial SiC film lead to the high catalytic activity toward HER and eventually the highest current density.

The recorded  $I$ - $t$  plots at  $-0.7$  V (vs. Ag/AgCl) under chopped light illumination (Figure 4b) confirm again higher PEC performance of an epitaxial 3C-SiC film toward PEC hydrogen production than that of microcrystalline and nanocrystalline SiC films. It has to be pointed out that a nanocrystalline SiC film shows the best stability toward HER, and the current density remains unchanged in the measured time range. This is probably because more amorphous phases significantly facilitate the release of  $H_2$  bubbles from the electrode surface. However, for the microcrystalline and epitaxial SiC films, the current densities decrease clearly at the first few circles of  $I$ - $t$  curves. This is related with the fact that the reduction of the specific surface areas of these SiC films originated from the aggregation of bubbles leads to their decreased catalytic activity. Moreover, both films have smaller  $R_{ct}$  values under illumination than those in the dark (Figure 4c). The  $R_{ct}$  values of three SiC photocathodes under light illumination follow an ascending order: epitaxial ( $17 \Omega$ ) < microcrystalline ( $30 \Omega$ ) < nanocrystalline ( $41 \Omega$ ). In other words, an epitaxial 3C-SiC photocathode features higher PEC activity toward HER.

## Conclusion

In summary, an epitaxial 3C-SiC film presents superior PEC activity for hydrogen evolution, including a higher current density, and faster charge transport kinetics than those of microcrystalline and nanocrystalline 3C-SiC films. Its excellent PEC properties originate mainly from its low electrical resistance and broad UV/Vis absorption. Together with its ideal energy level, photogenerated carrier recombination is hindered and the charge transport kinetics for photoelectrochemical water splitting is accelerated. The perfect (001) orientation and the higher phase purity of an epitaxial 3C-SiC film further improve PEC activity. Future work can be conducted to clarify deeply

photoelectrochemical reaction mechanisms on SiC photocathodes and to further improve PEC performance of an epitaxial 3C-SiC film through selected surface functionalization. An epitaxial 3C-SiC film is thus a promising photocatalyst to be employed in photoelectron devices and for efficient water-splitting applications.

## Experimental Section

**Chemicals and reagents:**  $H_2O_2$  (35%) and HF ( $\geq 48\%$ ) were purchased from Sigma-Aldrich Chemical Reagent Co., Ltd. (Beijing, China).  $H_2SO_4$  and ethanol were bought from Sinopharm Chemical Reagent Co., Ltd. (Shanghai, China). Insulation glue was obtained from Johnson Matthey Chemicals Co., Ltd. (Shanghai, China). All chemicals were used as received without further purification. Water ( $> 18 M\Omega$ ) was provided by a Millipore system.

**Material synthesis and characterization:** Three kinds of 3C-SiC films (namely epitaxial, microcrystalline and nanocrystalline 3C-SiC films) were synthesized in a microwave plasma chemical vapor deposition (MWCVD) reactor in a mixture of  $H_2$  and tetramethylsilane (TMS). By varying the deposition parameters, such as microwave power, gas pressure, substrate temperature (monitored by an optical pyrometer) and gas phase composition, 3C-SiC films with different structures were synthesized.<sup>[12]</sup> A JSM-7001F field emission scanning electron microscope (FESEM) was applied to analyze the structures and morphologies of three SiC films. The phase compositions and orientations of these SiC samples were acquired using a Bruker D8 advance A25X-ray diffraction (XRD) system. The phase purity of the films was determined by their Raman spectra collected on a HORIBA Jobin Yvon LabRAM HR800 spectrometer. And a 514.5 nm Ar laser was used as the excitation source. These SiC films were cleaned in piranha solution ( $H_2SO_4:H_2O_2=3/1$ ) and then in 5% HF solution to remove the surface contaminations and  $SiO_2$  surface layer prior to use.

**Optical measurements:** Diffusive reflectance UV/Vis absorption spectra were recorded on a UV-3600 spectrophotometer (Shimadzu, Japan).  $Al_2O_3$  acted as the reference. The Tauc plot ( $(\alpha hv)^{1/n}$  vs.  $hv$ ) was converted according to the Tauc equation [Eq. 1]:

$$\alpha hv = A(hv - E_g)^n \quad (1)$$

in which  $\alpha$  is the absorption coefficient,  $h$  is the Planck's constant,  $\nu$  is the frequency of incident light. Given that the transition belongs to indirect transition for an epitaxial 3C-SiC film,  $n$  is equal to 2.  $E_g$ , the bandgap of an epitaxial 3C-SiC film was then extracted

from the intercept of the Tauc plot. Photoluminescence spectra were measured by using an F-7000 (Hitachi, Japan) spectrophotometer with a Xe lamp as the excitation light source at room temperature.

**PEC water-splitting measurements:** All PEC tests were performed on a CHI 760 electrochemical workstation (CH Instruments, Inc., Shanghai, China) with a three-electrode configuration. A 3C-SiC film, a graphite rod electrode, and a Ag/AgCl electrode were served as the photocathode, counter electrode, and reference electrode, respectively. The area of the working electrode is 0.5 cm<sup>2</sup>. Prior to electrochemical measurements, the electrolyte solution (0.5 M H<sub>2</sub>SO<sub>4</sub>) was purged with high-purified argon for 30 min. The illumination source was a 150 W Xe lamp (PLS-SXE300C/CUV, Beijing Perfect Light Scientific and Technical Co. Ltd) with a power density of 100 mW cm<sup>-2</sup>. Current-voltage (*J*-*V*) curves were measured by means of linear sweep voltammetry (LSV) at a scan rate of 5 mV s<sup>-1</sup> under chopped light illumination. Moreover, the amperometric *I*-*t* curves were recorded at a potential of -0.7 V (vs. Ag/AgCl) and with the test duration of 500 s.

**Electrochemical impedance spectroscopy (EIS)** was carried out on a Zahner electrochemical workstation (Germany) in a frequency range from 100 kHz to 0.01 Hz at -0.7 V (vs. Ag/AgCl). Mott-Schottky plot was measured in a potential range from 0.2 to 1.5 V (vs. Ag/AgCl) at a frequency of 1 kHz without illumination. The flat-band potential was obtained according to [Eq. 2]:

$$\frac{1}{C^2} = \frac{2}{eN_d \epsilon \epsilon_0} \left[ E - E_{fb} - \frac{kT}{e} \right] \quad (2)$$

in which *C* is the capacitance of a space charge layer, *e* is the electric charge, *N<sub>d</sub>* is the donor density, *ε* is the dielectric constant of the semiconductor, *ε<sub>0</sub>* is the permittivity of vacuum, *E* is the applied potential, *E<sub>fb</sub>* is the flat-band potential, and *kT/e* is the temperature-dependent term.

## Acknowledgements

The authors acknowledge the financial support from Joint Funds the National Natural Science Foundation (U1710112), the financial support from the German Research Foundation (DFG) under project YA344/1-1, and the financial support from the China Scholarship Council (Award No. 201804910466).

## Conflict of interest

The authors declare no conflict of interest.

**Keywords:** hydrogen evolution reaction • photoelectrochemistry • silicon carbide • visible light • water splitting

- [1] M. Grätzel, *Nature* **2001**, *414*, 338–344.  
 [2] a) C. Y. He, X. L. Wu, J. C. Shen, P. K. Chu, *Nano Lett.* **2012**, *12*, 1545–1548; b) Q. Shen, J. Ma, X. F. Huang, N. J. Yang, G. H. Zhao, *Appl. Catal. B* **2017**, *219*, 45–52.  
 [3] S. U. M. Khan, M. Al-Shahry, W. B. Ingler, *Science* **2002**, *297*, 2243–2245.  
 [4] A. Paracchino, V. Laporte, K. Sivula, M. Gratzel, E. Thimsen, *Nat. Mater.* **2011**, *10*, 456–461.  
 [5] X.-L. Zheng, J.-P. Song, T. Ling, Z. P. Hu, P.-F. Yin, K. Davey, X.-W. Du, S.-Z. Qiao, *Adv. Mater.* **2016**, *28*, 4935–4942.  
 [6] T. Hisatomi, J. Kubota, K. Domen, *Chem. Soc. Rev.* **2014**, *43*, 7520–7535.  
 [7] Q. Wang, J. Y. Huang, H. T. Sun, K.-Q. Zhang, Y. K. Lai, *Nanoscale* **2017**, *9*, 16046–16058.  
 [8] C. Zhu, C. A. Liu, Y. J. Zhou, Y. J. Fu, S. J. Guo, H. Li, S. Q. Zhao, H. Huang, Y. Liu, Z. H. Kang, *Appl. Catal. B* **2017**, *216*, 114–121.  
 [9] A. Kojima, K. Teshima, Y. Shirai, T. Miyasaka, *J. Am. Chem. Soc.* **2009**, *131*, 6050–6051.  
 [10] a) R. A. Sayed, S. E. Abd El Hafiz, N. Gamal, Y. Gadelhak, W. M. A. El Rouby, *J. Alloys Compd.* **2017**, *728*, 1171–1179; b) K. Han, Y.-C. Lin, C.-M. Yang, R. Jong, G. Mul, B. Mei, *ChemSusChem* **2017**, *10*, 4510–4516.  
 [11] A. Kudo, Y. Miseki, *Chem. Soc. Rev.* **2009**, *38*, 253–278.  
 [12] H. Zhuang, N. J. Yang, L. Zhang, R. Fuchs, X. Jiang, *ACS Appl. Mater. Interfaces* **2015**, *7*, 10886–10895.  
 [13] H. Zhuang, L. Zhang, T. Staedler, X. Jiang, *Chem. Vap. Deposition* **2013**, *19*, 29–37.  
 [14] F. Demichelis, C. F. Pirri, E. Tresso, G. D. Mea, V. Rigato, P. Rava, *Semicond. Sci. Technol.* **1991**, *6*, 1141–1146.  
 [15] W. J. Choyke, *Mater. Res. Bull.* **1969**, *4*, 141–152.  
 [16] S.-C. Chiu, Y.-Y. Li, *J. Cryst. Growth* **2009**, *311*, 1036–1041.  
 [17] X. F. Huang, Q. Shen, J. B. Liu, N. J. Yang, G. H. Zhao, *Energy Environ. Sci.* **2016**, *9*, 3161–3171.  
 [18] J. B. Liu, H. J. Shi, Q. Shen, C. Y. Guo, G. H. Zhao, *Appl. Catal. B* **2017**, *210*, 368–378.  
 [19] a) F. Y. Ning, M. F. Shao, S. M. Xu, Y. Fu, R. K. Zhang, M. Wei, D. G. Evans, X. Duan, *Energy Environ. Sci.* **2016**, *9*, 2633–2643; b) H. Kaneko, T. Minegishi, M. Nakabayashi, N. Shibata, K. Domen, *Angew. Chem. Int. Ed.* **2016**, *55*, 15329–15333; *Angew. Chem.* **2016**, *128*, 15555–15559.  
 [20] J. T. Song, T. Iwasaki, M. Hatano, *Jpn. J. Appl. Phys.* **2014**, *53*, 05FZ04.  
 [21] R. Subbaraman, D. Tripkovic, D. Strmcnik, K. C. Chang, M. Uchimura, A. P. Paulikas, V. Stamenkovic, N. M. Markovic, *Science* **2011**, *334*, 1256–1260.

Manuscript received: November 18, 2019

Accepted manuscript online: January 21, 2020

Version of record online: March 3, 2020